scientific reports

Check for updates

OPEN

A multi-technique approach to understanding delithiation damage in $LiCoO_2$ thin films

E. Salagre[1], S. Quílez[1], R. de Benito[1], M. Jaafar[1,2], H. P. van der Meulen[3,4], E. Vasco[5], R. Cid[5,6,7], E. J. Fuller[8], A. A. Talin[8], P. Segovia[1,2,4], E. G. Michel[1,2,4] & C. Polop[1,2,4]✉

We report on the delithiation of $LiCoO_2$ thin films using oxalic acid ($C_2H_2O_4$) with the goal of understanding the structural degradation of an insertion oxide associated with Li chemical extraction. Using a multi-technique approach that includes synchrotron radiation X-ray diffraction, scanning electron microscopy, micro Raman spectroscopy, photoelectron spectroscopy and conductive atomic force microscopy we reveal the balance between selective Li extraction and structural damage. We identify three different delithiation regimes, related to surface processes, bulk delithiation and damage generation. We find that only a fraction of the grains is affected by the delithiation process, which may create local inhomogeneities. However, the bulk delithiation regime is effective to delithiate the LCO film. All experimental evidence collected indicates that the delithiation process in this regime mimics the behavior of LCO upon electrochemical delithiation. We discard the formation of Co oxalate during the chemical extraction process. In conclusion, the chemical route to Li extraction provides additional opportunities to investigate delithiation while avoiding the complications associated with electrolyte breakdown and simplifying in-situ measurements.

Lithium-ion batteries (LIBs) are widely used in current consumer electronics, and their demand in electric and hybrid vehicles as also for powering the internet of the things (IoT) is expected to grow rapidly in the near future[1,2]. The most common cathode material in LIBs for consumer electronics is lithium cobalt oxide (Li_xCoO_2, LCO). LCO crystallizes in the α-$NaFeO_2$ structure, a layered rock-salt structure made up of alternating layers of CoO_2 and Li[3]. The layered structure allows a high mobility for Li atoms that enables LCO to reversibly intercalate Li. This feature is behind the excellent properties of LCO as a Li storage material in rechargeable LIBs, where the Li content can change by up to ~ 40% during the battery charging/discharging in a standard electrochemical process[4,5]. Despite decades of research, questions remain regarding damage associated with Li insertion and extraction, reflecting the complex and interrelated processes involving electronic, chemical and structural aspects of the cathode materials[6]. Electrochemical Li extraction is frequently used to produce LCO films with different Li content, which can then be subjected to various types of ex situ analysis. While attractive in many respects, electrochemical Li extraction can also present numerous challenges including electrochemical side reactions related to electrolyte degradation and strong dependence of reaction rates on local electronic conductivity. Alternatively, chemical delithiation methods are significantly simpler experimentally, can be tuned to remove precise Li content using reactant concentration, and are independent of the local cathode electronic conductivity[7,8]. In turn, a dilute acid solution in contact with LCO extracts Li, but it may also extract Co and induce an irreversible damage in the structure[9].

Previously, it was found that structural effects produced by both electrochemical and chemical delithiation methods are similar, i.e. the lattice constants and other structural parameters of chemically delithiated LCO are in good agreement with those of LCO delithiated by electrochemical methods for a significant delithiation range[5]. Nonetheless, other aspects such as the activity for the oxygen evolution reaction depend on the Li extraction method used[10]. Furthermore, chemical delithiation is in general studied for LCO particle-based electrodes,

[1]Departamento de Física de la Materia Condensada, Universidad Autónoma de Madrid, Madrid, Spain. [2]IFIMAC (Condensed Matter Physics Center), Universidad Autónoma de Madrid, Madrid, Spain. [3]Departamento de Física de Materiales, Universidad Autónoma de Madrid, Madrid, Spain. [4]Instituto Universitario de Ciencia de Materiales Nicolás Cabrera, Universidad Autónoma de Madrid, Madrid, Spain. [5]Instituto de Ciencia de Materiales de Madrid, Consejo Superior de Investigaciones Científicas, Madrid, Spain. [6]BM25-SpLine (Spanish CRG Beamline) at the European Synchrotron (E.S.R.F.), Grenoble, France. [7]Centre for Cooperative Research on Alternative Energies (CIC energiGUNE), Basque Research and Technology Alliance (BRTA), Vitoria-Gasteiz, Spain. [8]Sandia National Laboratories, Livermore, CA, USA. ✉email: celia.polop@uam.es

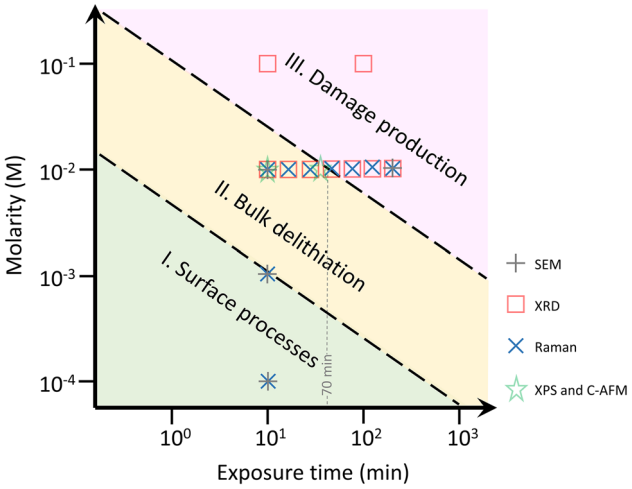

Figure 1. Overview of the different chemical delithiation regimes of LCO thin films with a diluted solution of oxalic acid. Symbols represent the parameters of acid concentration and exposure time that have been used in the experiments. Dashed lines tentatively separate the regions of the parameter space of the different regimes.

which can be challenging to interpret due to their heterogeneity and the presence of organic binders and electronic conductivity additives. Thin-films on the other hand, do not contain such additives and are much more amenable to investigation using traditional surface science and scanning probe methods. Among the different acids employed in chemical delithiation, oxalic acid ($C_2H_2O_4$) has been reported to be the most selective for removing Li ions from LCO cathodes with minimal extraction of Co[9]. Zheng et al. have proposed the following reaction to describe the process[11],

$$5C_2H_2O_{4(l)} + 2LiCoO_{2(s)} \rightarrow 2LiHC_2O_{4(l)} + 2CoC_2O_{4(s)} + 4H_2O_{(l)} + 2CO_{2(g)} \quad (1)$$

This reaction produces $LiHC_2O_4$, which is moderately soluble in H_2O, and Co oxalate CoC_2O_4, which precipitates. However, there is no agreement on the effectiveness of this procedure and its consequences on the structural integrity of the LCO lattice[12].

In this work, we investigate the processes of chemical delithiation and associated structural defect formation in cathodes of LCO thin films with the goal of understanding the chemical delithiation route and the degradation processes involved in it, determining the balance between selective Li extraction and structural damage and to correlate results obtained using experimental techniques sensitive to different properties of the LCO thin layer. In this approach we analyze strictly the role of oxalic acid and eliminate the side effects related to the presence of mixed electrodes (e.g. including PVDF, conducting carbon, etc.). Thin films of $LiCoO_2$ grown by magnetron sputtering are exposed ex-situ to oxalic acid ($C_2H_2O_4$). The processes of structural changes and damage to the LCO films are investigated using synchrotron radiation powder XRD (X-Ray Diffraction), XPS (X-ray Photoelectron Spectroscopy), SEM (Scanning Electron Microscopy), micro Raman spectroscopy and C-AFM (Conductive Atomic Force Microscopy). We report the existence of three different regimes, each dominated by a characteristic type of process: surface processes, bulk delithiation and damage generation. We define the different balance between Li extraction and formation of structural damage that characterizes each regime during the chemical delithiation of LCO. We find that chemical delithiation is observed for a range of moderate acid concentrations and exposure times. Under these conditions, Li is selectively extracted after exposing LCO films. The structural and electrical properties of the resulting LCO films are similar to electrochemically delithiated LCO. The chemical route to Li extraction provides additional opportunities to investigate delithiation while avoiding complications associated with electrolyte breakdown and simplifying in-situ measurements.

Results and discussion

The reaction of oxalic acid with LCO films defines three delithiation regimes for the concentration and exposure times probed, as shown in Fig. 1. Low concentration ($\leq 10^{-3}$ M) and short exposure times (≤ 10 min) correspond to Regime I, defined by the presence of surface processes only. In Regime II (moderate concentrations of 10^{-2} M and times below 70 min) bulk delithiation is observed. Larger exposure times (≥ 100 min) at concentrations of 10^{-2} M and larger correspond to Regime III, where lattice damages are observed. These damages provide us with a measure of the loss of selectivity of the leaching reaction. The features of each regime are described in more detail in the following.

SEM provides an overview of the LCO film morphology in different delithiation regimes as a function of the exposure conditions. The evolution of delithiation-induced features is summarized in Fig. 2. The as-grown film shows a typical polycrystalline morphology characterized by dispersed faceted grains with an average size of 60 nm (Fig. 2a). A mild exposure to oxalic acid with a molar concentration of 10^{-4} M induces changes in the surface of the grains, which coalesce into bundles (regions enclosed by a dashed green contour in Fig. 2b,c). These surface structures grow with the exposure time, reaching an average size of 90 nm for 10 min-exposure.

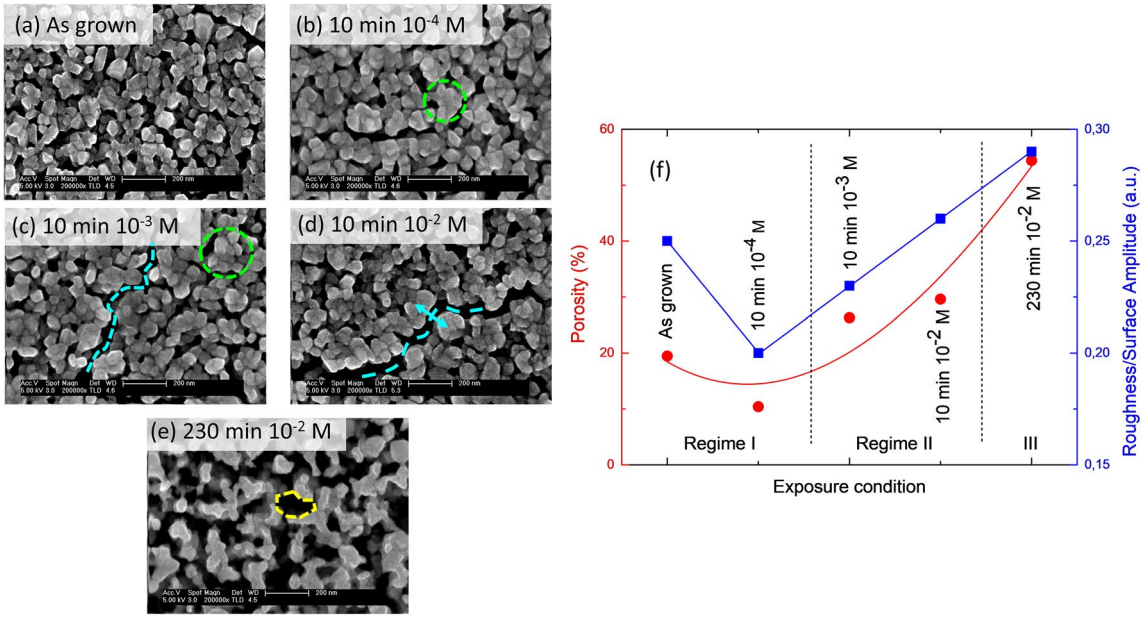

Figure 2. Evolution of the LCO thin film structure imaged by SEM for different exposure conditions to oxalic acid. Scale bar in (**a**–**e**) corresponds to 200 nm. Regions enclosed by a dashed green contour in (**b**) and (**c**) correspond to bundles of coalescing grains. Dashed light blue curves in (**c**) and (**d**) depict grooves. The blue arrow in (**d**) highlights the widening of the grooves. The dashed yellow section in (**e**) highlights the cross-section of a channel. (**f**) Roughness and film porosity for different exposure conditions. Curves serve as a visual guide. Figure created with WSxM 5.0 Develop (http://www.wsxm.es)[15].

The size increase is due mainly to the grouping of grains, rather than to their slight coarsening, as demonstrated by a statistical analysis using self-correlation (ACO) and power spectral density (PSD) functions (Fig. S2 in Suppl. Info.). The larger surface structures cause both the film roughness and porosity to decrease slightly, as shown in Fig. 2f. These changes are likely due to the surface delithiation of the grains (Regime I in Fig. 1), as this process will affect first the surface morphology of the grains. The separation between surface roughness and bulk porosity coming to the surface is done by fitting the height distribution of the calibrated images using an outer Gaussian function centered on the average thickness (i.e., the mode of the height distribution) and an asymmetric background that corresponds to the tail of the distribution of emerging porosity (Fig. S3 in Suppl. Info.). We have ruled out that the surface phenomenon inducing an initial decrease in both porosity and roughness is an effect of distilled water used as a solvent. Exposure of LCO films to distilled water without acid produces a grain dispersion rather than a bundling, which results in a contrary behavior of roughness, i.e., roughness increases.

As the acid concentration is increased up to 10^{-3} M, we begin to observe bulk delithiation by XRD and Raman (see below). The coexistence of both surface and bulk processes produces bundles of grains separated by deep grooves (dashed light blue curve in Fig. 2c). This increases the roughness and porosity of the LCO films. Longer exposure times at lower concentrations and/or a further increase in the exposure concentration (10^{-2} M) enhance the bulk delithiation (Regime II in Fig. 1), widening the grooves, as shown by the dashed light blue curve and blue arrow in Fig. 2d.

Longer exposures and higher acid concentrations substantially increase the observed damage (Regime III). The increased porosity gives rise to a network of channels (dashed yellow section in Fig. 2e), resulting in a high-specific surface area morphology. In addition to homogeneous damage throughout the film (regions A in Fig. 3), we also observe highly localized features such as expelled material and pits (regions B).

We have performed grazing incidence XRD in-plane measurements for as-grown samples and after successive oxalic acid exposures, in order to investigate the structural changes of LCO upon delithiation. We have monitored the main X-ray reflections for LCO, specifically (003), (104), (101), (10–5) and (107) during the process. The structure of as-grown LCO is rhombohedral (R-3 m space group), but is typically described with a hexagonal structure as this is easier to visualize, usually labelled hex-I. Previous work has shown that delithiation causes structural phase transitions[4,16,17]. The hex-I phase of as-grown LCO is observed for Li concentrations in the range $0.95 \leq x \leq 1$. In the range $0.75 \leq x \leq 0.95$ there is phase coexistence between the hex-I phase and a second phase (called hex-II) with lower Li contents. The hex-II phase has similar atomic positions as hex-I, but has a larger *c* lattice constant, due to the partial removal of Li. In the range $0.50 \leq x \leq 0.75$, only the hex-II phase is observed. Near $x = 0.5$, a new phase of monoclinic symmetry appears. This phase is the result of a monoclinic distortion of the hexagonal lattice and is traced back to the ordering of Li ions within the Li layers[4,17] (see Suppl. Info., Sect. 6). The hex-I phase corresponding to as-grown LCO is electrically insulating, while the hex-II phase is metallic, so that an insulator–metal phase transition is observed when the Li contents decreases[16,18,19]. Figure 4 shows an XRD spectrum characteristic of LCO. The X-ray reflections are indexed according to a hexagonal lattice. Several residual reflections from the Pt layer underneath the LCO film and the Si substrate are also detected. XRD spectra after 10 min and after 150 min of exposure to 10^{-2} M oxalic acid are also shown, corresponding to Regime II

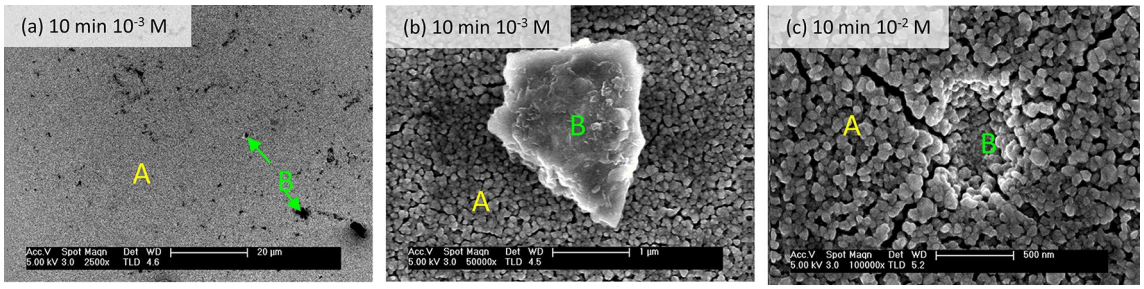

Figure 3. Homogeneous and heterogeneous damages (regions labelled A and B, respectively) in LCO thin films caused by exposures to oxalic acid. Scale bars correspond to: (**a**) 20 µm, (**b**) 1 µm and (**c**) 500 nm. Figure created with WSxM 5.0 Develop (http://www.wsxm.es)[15].

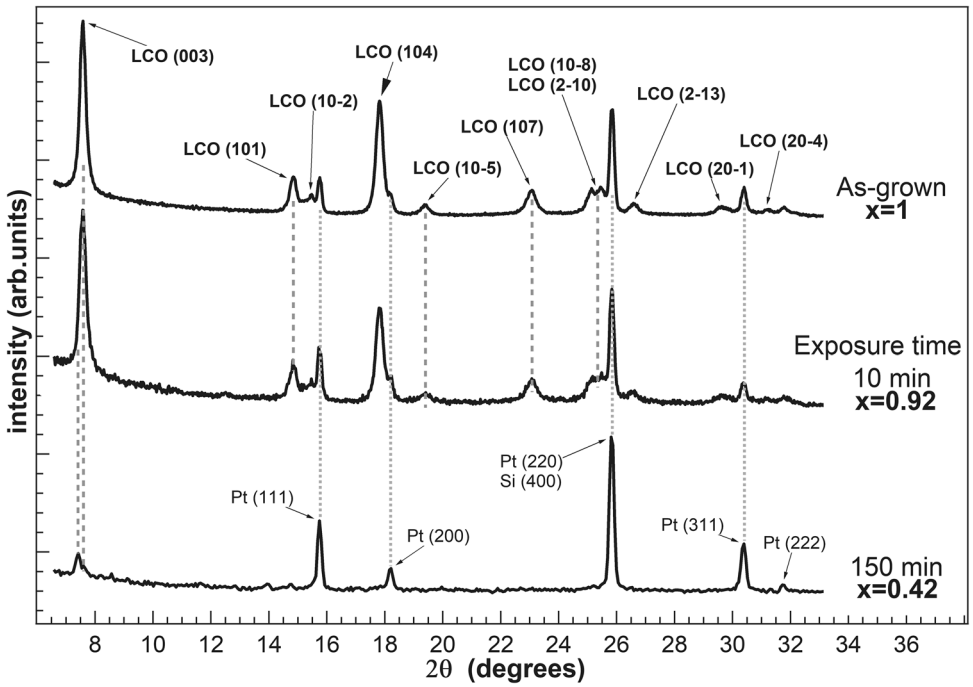

Figure 4. X-ray powder diffraction spectra corresponding to the as-grown LCO structure (top) and to samples delithiated 10 min (center) and 150 min (bottom) in 10^{-2} M oxalic acid. Reflections are indexed in the hexagonal structure. Residual reflections from the Pt layer underneath the LCO film and the Si substrate are detected.

(bulk delithiation) and Regime III (damage), respectively. As the film density decreases due to exposure to oxalic acid, more X-rays are able to penetrate to the substrate, and a significant increase of Pt and substrate peaks is observed for 150 min exposure time. The formation of pits in the LCO film also contribute to this effect. Note that no signal of crystalline Co oxalate is detected[11,20,21] (see Fig. S4 in Suppl. Info.).

Figure 5a shows the evolution of the (003) reflection as a function of exposure time to oxalic acid (10^{-2} M). The (003) reflection probes directly the *c* lattice constant of the hexagonal structure. Li deintercalation produces a splitting of the (003) peak, due to the appearance of the hex-II structure with a larger *c* lattice constant. The coexistence of the two structures hex-I and hex-II is in agreement with previous findings[22,23]. Figure 5b shows the deconvolution of selected (003) reflections. Two dominant peaks are required to reproduce the line profile, one corresponding to the hex-I phase (blue) and one from the hex-II phase (orange). Two minor additional contributions have to be added, one corresponding to residual Co_3O_4 (green) and another one to account for strongly delithiated areas in the sample (magenta), due to local inhomogeneity[23]. The evolution of the dominant hex-I and hex-II components follows the expected behavior, from a dominant hex-I peak for the as-grown sample, to a dominant hex-II after strong delithiation. For each exposure time, the relative intensities of each component are represented as percentage of the total intensity of the (003) reflection for that particular time in Fig. 5c. Note that the decrease of hex-I is related to the concomitant increase of hex-II and of the residual Co oxide signal. The data corresponding to exposure times below 70 min ($x \approx 0.6$) correspond to regime II (bulk delithiation), while data above 70 min correspond to regime III (damage), which is characterized in XRD data by the increase of

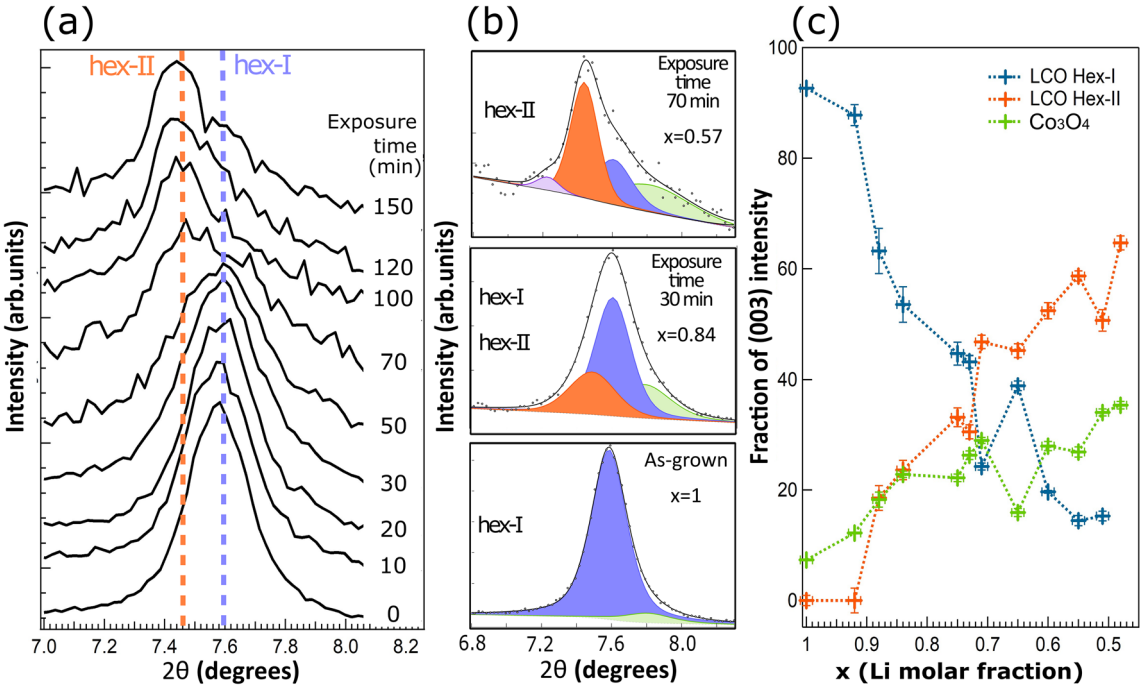

Figure 5. (**a**) Evolution of the (003) reflection in grazing incidence powder diffraction for increasing exposure times at 10^{-2} M concentration. Note the splitting of the peak due to the coexistence of the hex-I and hex-II structures with different c lattice parameter and the shift of the maximum to lower angles as the exposure time increases. (**b**) Deconvolution of selected peaks corresponding to the (003) reflection including hex-I (blue), hex-II (orange), Co_3O_4 (green), and residual strongly delithiated areas (magenta). (c) Intensity of the different components (hex-I, hex-II and Co_3O_4) in the (003) reflection as a function of Li molar fraction. For each exposure time, the relative intensities of components are normalized with respect to the total intensity of the (003) reflection for that particular exposure time. Figure created with Igor Pro 6.3.7.2 (Wavemetrics, Lake Oswego, OR, USA, https://www.wavemetrics.com) and Inkscape 1.0.2 (Copyright (C) 1989, 1991 Free Software Foundation, Inc. 51 Franklin Street, Fifth Floor, Boston, MA 02110-1301, USA, https://inkscape.org/es).

signal coming from Co oxide and substrate peaks (Pt, Si), due to the formation of significant pits and channels in the LCO film as imaged by SEM.

Figure 6a (top) displays the values of the *c* lattice parameter as a function of delithiation time and Li molar fraction obtained from the data in Fig. 5. The results are compared to measurements of the *c* lattice parameter for single-crystalline samples of Li_xCoO_2 of well-defined composition[24]. There is an overall good agreement between both sets of data, showing that the variation in lattice parameter *c* is consistent with the coexistence of hex-I and hex-II phases region for $0.75 < x < 0.95$. It is important to note that the chemical delithiation results in a heterogeneous phase transformation. This is deduced from Fig. 5, as the hex-I component persists for x values lower than reported (down to 0.5 instead of 0.75). Another clue leading to this conclusion is that the line profile of the (003) peak corresponding to a large delithiation ($x = 0.57$, Fig. 5b, top peak), shows a shoulder on its low angle side, indicating that some sample areas have lower lithium concentration than average. Overall, the values for the parameter *c* of the hex-II phase are slightly higher than reported, probably due to this heterogeneous Li deintercalation. Figure 6a (bottom) shows the corresponding values of the *a* lattice parameter of the hexagonal cell as a function of delithiation time and Li molar fraction. As in Fig. 6a (top), the results are compared to measurements of the *a* lattice parameter for samples of Li_xCoO_2 of well-defined composition[17]. While the values of *a* for high Li molar fractions ($x > 0.8$) are in perfect agreement with previous results[17], the values observed in the case of smaller Li molar fractions ($x < 0.8$) are slightly larger (between 0.02 and 0.03 Å).

Figure 6b shows the intensity of different X-ray reflections as a function of exposure time and Li molar fraction, as determined from the (003) peak position. The intensities are normalized to the incident radiation intensity. Figure 6b highlights the evolution from bulk delithiation towards damage. An almost linear decrease of the intensities is observed as a function of the exposure time in the range for $0.5 < x < 1$. In this range, the bulk delithiation takes place, as deduced from the analysis of the *c* lattice constant. Interestingly, the evolution of the lattice parameters of both the phase hex-I and hex-II follows closely the behavior found for electrochemical delithiation or for single crystals[4,24]. Damage is gradually introduced, as evidenced by the drop in intensity for all reflections (Fig. 6b), which become residual with respect to the substrate contribution above 60–70 min (Regime III). The damage is also evidenced from the growth of the relative importance of Co oxide peaks (Fig. 5). These results agree with the morphological description obtained by SEM.

Figure 7 shows a series of Raman spectra obtained for increasing exposure times at 10^{-2} M oxalic acid solution. A typical Si substrate coated only by a Pt/Ti buffer layer was measured as well. No signal was observed in the analyzed range, which demonstrates that Pt/Ti completely shields the 520 cm^{-1} Si signal. The two most

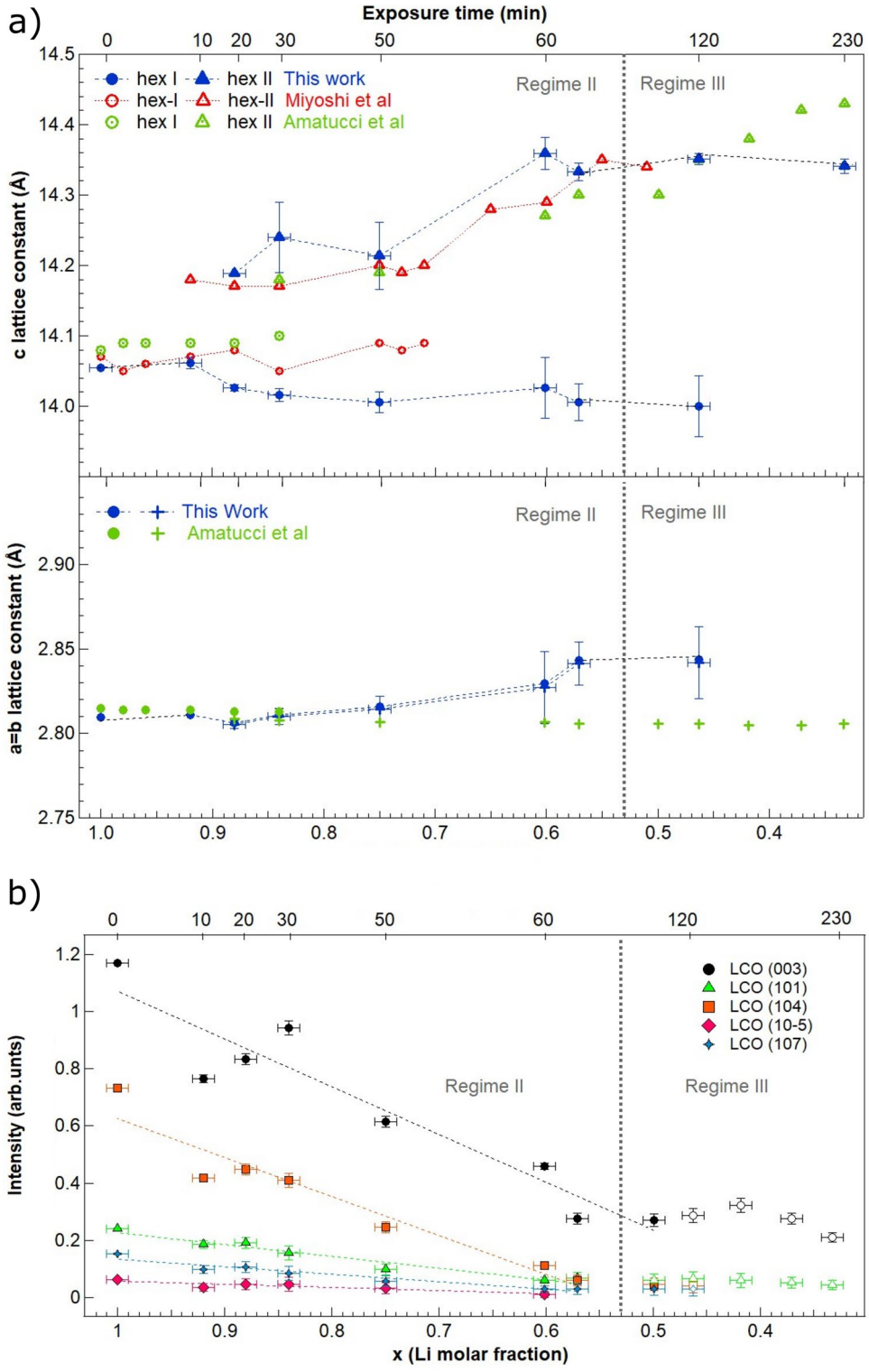

Figure 6. Dependences of (**a**) lattice parameter *c* and *a* for Li_xCoO_2 and (**b**) the intensities of X-ray reflections on the exposure time at 10^{-2} M concentration (top axis) and Li molar fraction (bottom axis). The appearance of *c* and *a* values are compared to literature values reported in Ref.[17,24].

prominent peaks in Fig. 7a correspond to the A1g and Eg modes of LCO. No changes in the Raman spectra are visible in Regime I, corresponding to lower acid concentrations and shorter exposure times (not shown). In Regime II (up to 70 min of exposure time at 10^{-2} M), the overall intensity of the spectra slowly increases and

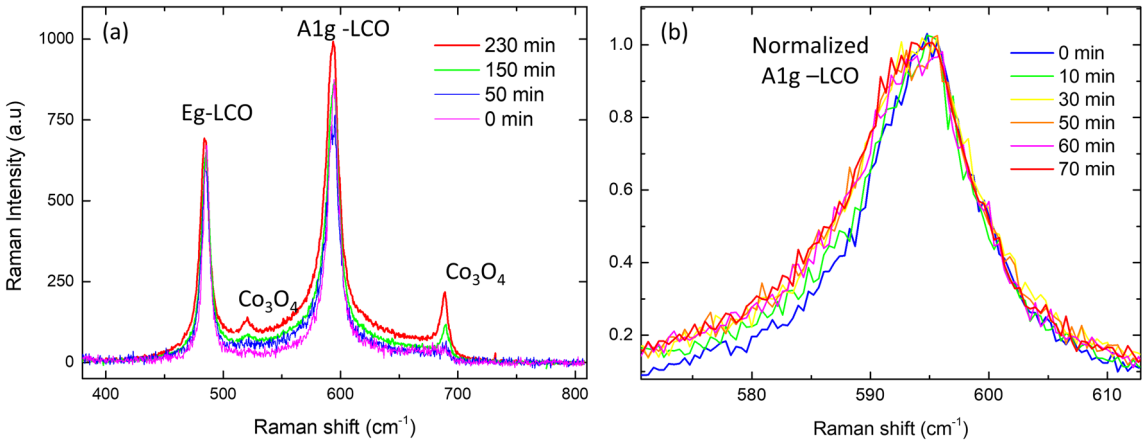

Figure 7. (**a**) Evolution of the Raman spectra for various exposure times at a 10^{-2} M solution of oxalic acid. (**b**) Evolution of the A1g-LCO peak (normalized to the height) for exposure times up to 70 min (corresponding to Regime II). The broadening of the left side is due to the appearance of the hex-II phase of LCO.

a broadening of both the Eg (485 cm^{-1}) and the A1g (593 cm^{-1}) peaks is observed at their low-energy side, as illustrated in Fig. 7(b) for the A1g peak. This is ascribed to the gradual transformation of LCO from the hex-I to the hex-II phase, the latter having the Raman peaks at slightly lower energies[25,26]. A minor contribution from residual Co_3O_4 is also detected in Regime II (exposure times below 70 min). For exposure times beyond 70 min, corresponding to Regime III, peaks of Co_3O_4 increase as an indication that damage is introduced in the sample. The damage is also reflected in the higher contribution of the Raman signal in-between the peaks, which is a consequence of the appearance of structural disorder in the material. No Raman signal of Co oxalate has been detected, expected at a value of 783 cm^{-1}[27].

Figure 8 represents the Raman intensity vs. exposure time. The insert in Fig. 8a shows that the total integrated intensity stays constant in Regime I (exposure times of 10 min at 10^{-4} and 10^{-3} M acid concentration). In turn, the total integrated intensity grows continuously during Regime II and III (Fig. 8a). This enhancement in Raman efficiency can be explained both by an increase in the surface to volume ratio due to the porosity evolution as observed by SEM and by the change in the bandgap of the material as the Li-concentration diminishes[28]. The Regimes II and III are recognized in Fig. 8b,c, where the relative integrated contribution of the Eg Raman peak (summing up the two phases) is constant up to 70 min and decreases afterwards. The relative integrated contribution of the Co_3O_4 peak at 689 cm^{-1} shows the opposite behavior, i.e. an increase in Regime III when the damage sets in, in agreement with XRD results.

An interesting feature in the Raman spectra is the remarkable persistence of the hex-I phase until the maximum exposure time. In the XRD data both phases are observed until a Li molar fraction of at least 0.45 (Fig. 6), corresponding to a delithiation time of 120 min. The relative evolution of the intensities of the two phases is also different in both techniques. In the Raman spectra the phase II signal is always lower than that of phase I, while in XRD experiments the signal of phase II replaces the signal of phase I. On one hand, the persistence of the hex-I phase beyond 0.75 molar fraction indicates that the sample is not homogeneous after the chemical delithiation, in agreement with the observation by XRD of regions further impoverished in Li (Fig. 5b, top). On the other hand, we may expect that the Raman measurement is more sensitive to the surface layer. This is because the optical penetration depth is reduced by the presence of the metallic hex-II phase as well as by the increase in absorption because of an approaching resonance when the Li-concentration diminishes (the latter also can be responsible for the net increase in the Raman signal)[28]. The persistence of the hex-I phase is in contrast with results of Raman spectra taken in an electrochemical delithiation process, where the Raman signal of the hex-I phase disappears as the Li-content falls below 0.8[26]. The reason for the different behavior is presently unknown but may be due to how the LCO material is prepared and the uniformity of delithiation process.

In order to corroborate some of the results described above, complementary measurements by XPS and C-AFM were made in the as-grown sample and compared to results obtained in a delithiated sample in Regime II.

Full range XPS spectra are measured to check the sample composition and cleanliness. Figure 9 shows XPS spectra corresponding to Co 3p and Li 1s, which are used to determine the Li contents for the as-grown sample and for a chemically delithiated sample (65 min in 10^{-2} M oxalic acid corresponding to Regime II). The core levels are normalized to the maximum of Co 3p to highlight the changes. Co 3p is a doublet, but the splitting of the components is small and is not observed with our experimental resolution[29]. The peak presents an asymmetric shape as described in Ref.[22]. The analysis of the Li 1s core level is hindered by its low cross section for the photon energy used. The peak is difficult to observe, especially in delithiated samples. Nonetheless, its change upon delithiation is clear. Comparing with published results[22], the observed Li 1s and Co 3p peak ratios together with the decrease of Li 1s height correspond to a value of $x = 0.5$ for the delithiated sample, while for the as-grown sample the stoichiometry is close to $x = 1$, as expected. The result demonstrates that oxalic acid at low concentrations is able to partially remove Li from LCO without imparting structural damage. Therefore, the chemical reaction for Li extraction in Regime II can be written simply as

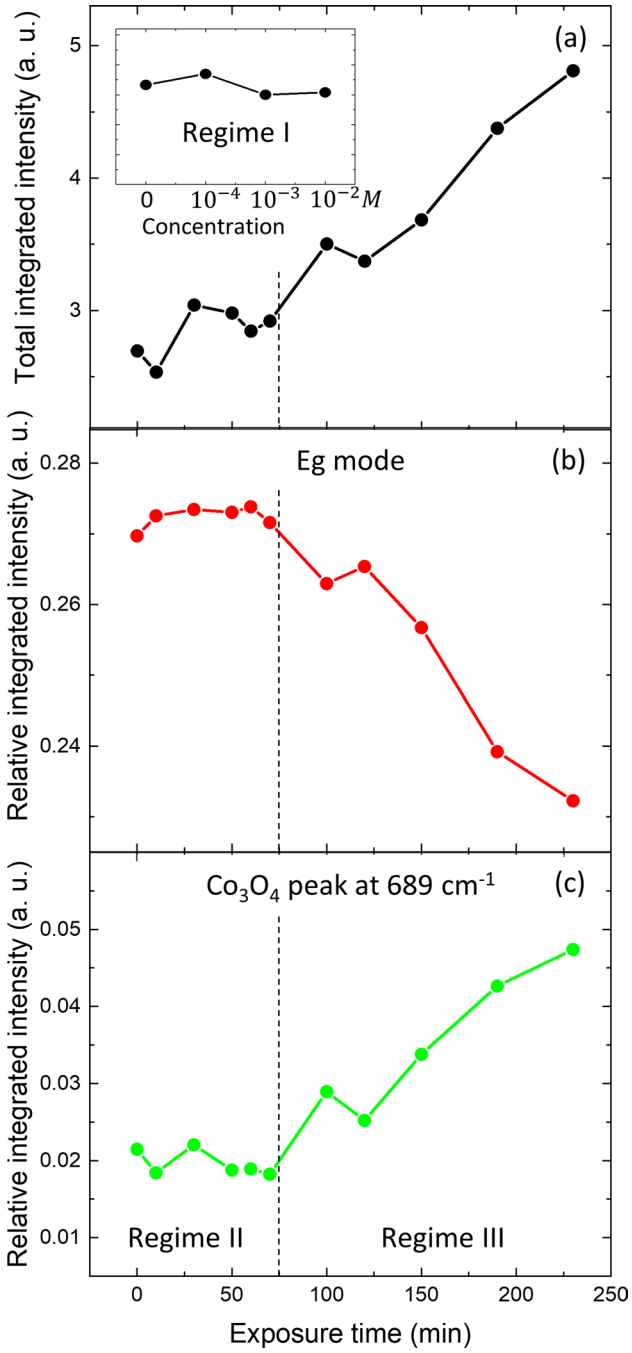

Figure 8. Evolution with exposure time at a 10^{-2} M acid concentration of: (**a**) the total integrated Raman spectrum, (**b**) the relative integrated contribution of the Eg Raman peak (summing up the 2 phases), and (**c**) the relative integrated contribution of the Co_3O_4 peak at 689 cm^{-1}. Regimes II (below 70 min.) and III (above 70 min) are clearly distinguishable in (**b**) and (**c**). The insert in (**a**) represents the total integrated Raman spectrum in Regime I: acid exposure times of 10 min at the lower concentrations.

$$xC_2H_2O_{4(l)} + LiCoO_{2(s)} \rightarrow Li_{1-x}CoO_{2(s)} + xLiHC_2O_{4(l)}$$

Previous studies have shown the influence of the delithiation process in the electronic conductivity of LCO. The hex-I phase corresponding to as-grown LCO is electrically insulating having the Co atoms in the 3 + state, while the hex-II phase is metallic due to the Li vacancies created during delithiation and the creation of holes in the valence band and consequently Co^{4+} ions[16, 18, 19]. So, an insulator–metal phase transition is observed when the Li contents decreases, which is the focus of an extensive debate. Thus, while Li_xCoO_2 is insulating for $x \geq 0.95$, a metallic conductivity appears for $0.35 \leq x \leq 0.95$[30]. Milewska and coworkers report an enhancement

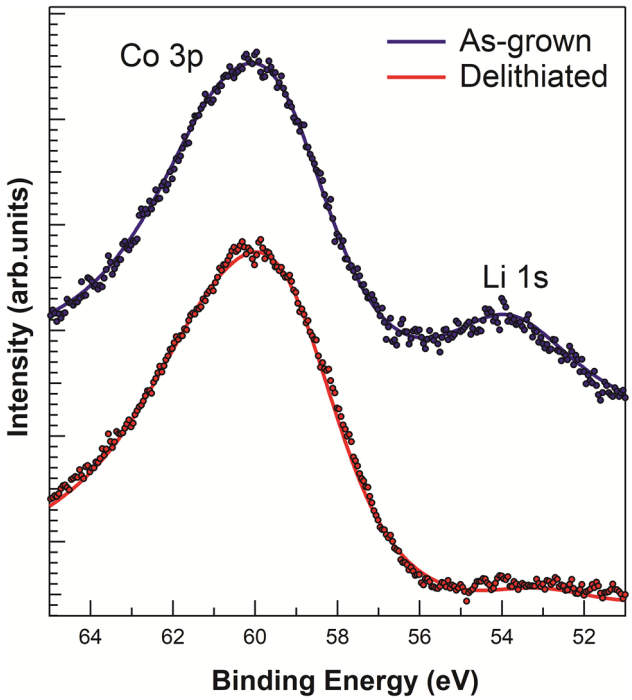

Figure 9. XPS Co 3p and Li 1s regions for the as-grown (top) and chemically delithiated (65 min at 10^{-2} M oxalic acid, bottom) samples. Dots are experimental data and the line serves as a guide to the eye.

of the electrical conductivity of 6 orders of magnitude upon electrochemical delithiation[18]. By comparing their results with other reports in the literature, they conclude that the electrical properties of thin LCO films differ from data obtained for powder LCO in terms of electrical conductivity. Moreover, a comparison between works using different preparation methods of LCO, which implies dissimilar structures of the material, may yield different behaviors[18].

Figure 10 shows a qualitative comparison of the electrical conductivity (by C-AFM) between the same samples analyzed previously by XPS. Both samples present the typical grain morphology (Fig. 10a,b and Fig. S5 in Suppl. Info.) consistent with SEM. The electrical current map measured at a bias of − 1.5 V in the as-grown sample, Fig. 10c, shows a moderately heterogeneous spatial distribution of low conductivity, likely due to the morphology of the polycrystalline films. In turn, the current map in the delithiated sample, Fig. 10d, shows a highly heterogeneous conductivity with enhanced regions, probably where delithiation is deeper. The increase in the heterogeneity, as revealed by the comparison in Fig. 10e of the widths of the corresponding histograms, is due to two effects: (1) the heterogeneous structure inherent to the polycrystalline film, and (2) the heterogeneity in the delithiation front, which are closely related to each other as suggested by the SEM measurements in Fig. 2. We have estimated typical conductivity values of the order of 10^{-2} S cm^{-1}, from current maps and taking into account tip-sample contact areas and sample thickness. The conductivity values are in the range of those previously reported for electrochemically delithiated LCO[18]. However, we note that we are using two-point method measurements, so that series resistance could affect them.

The multi-technique approach by using SEM, XRD, Raman, XPS and C-AFM reveals the existence of three regimes of chemical delithiation of the LCO film by exposure to oxalic acid, depending on the acid molar concentration and exposure time conditions, as shown in Fig. 1. The regimes differ in the morphology, structures, and chemical composition of the LCO film that result from the leaching reaction. Regime I corresponds to a mild surface delithiation causing a bundling of grains. A model to address this phenomenon is described in Suppl. Info (Sect. 5, Fig. S6a). In short, surface delithiation induces an inhomogeneous lattice expansion in the shell of the grain as the Li content falls[17]. This expansion preferably occurs on the free surface of the grains away from the contact sections between neighboring grains; and causes an increase in the specific surface of the grains. In thermodynamic terms, bundling counteracts this increase in specific surface to lower the system energy. Regime II is effective to delithiate the bulk of the LCO film, as evidenced by the changes in Li concentration, the appearance of phase hex-II and the evolution of the lattice constants of hex-I and hex-II phases. All these features mimic the behavior of LCO upon electrochemical delithiation[4,16–18], and that detected in single crystalline samples[24]. Additionally, in regime II, groove formation starts to occur. We interpret this effect as a result of the erosion caused by concentrated oxalic acid, which occurs preferentially in the surface sites with higher curvature (i.e., greater reactivity), namely, the triple-junction points between grains. The model in Suppl. Info. (Sect. 5, Fig. S6b) outlines the morphology evolution of a groove induced by leaching. Further acid exposure (Regime III) corresponds to increased structural degradation and amorphization of the LCO film, which produces high-specific surface area structures. However, rather than abrupt crossover between regimes, ranges of

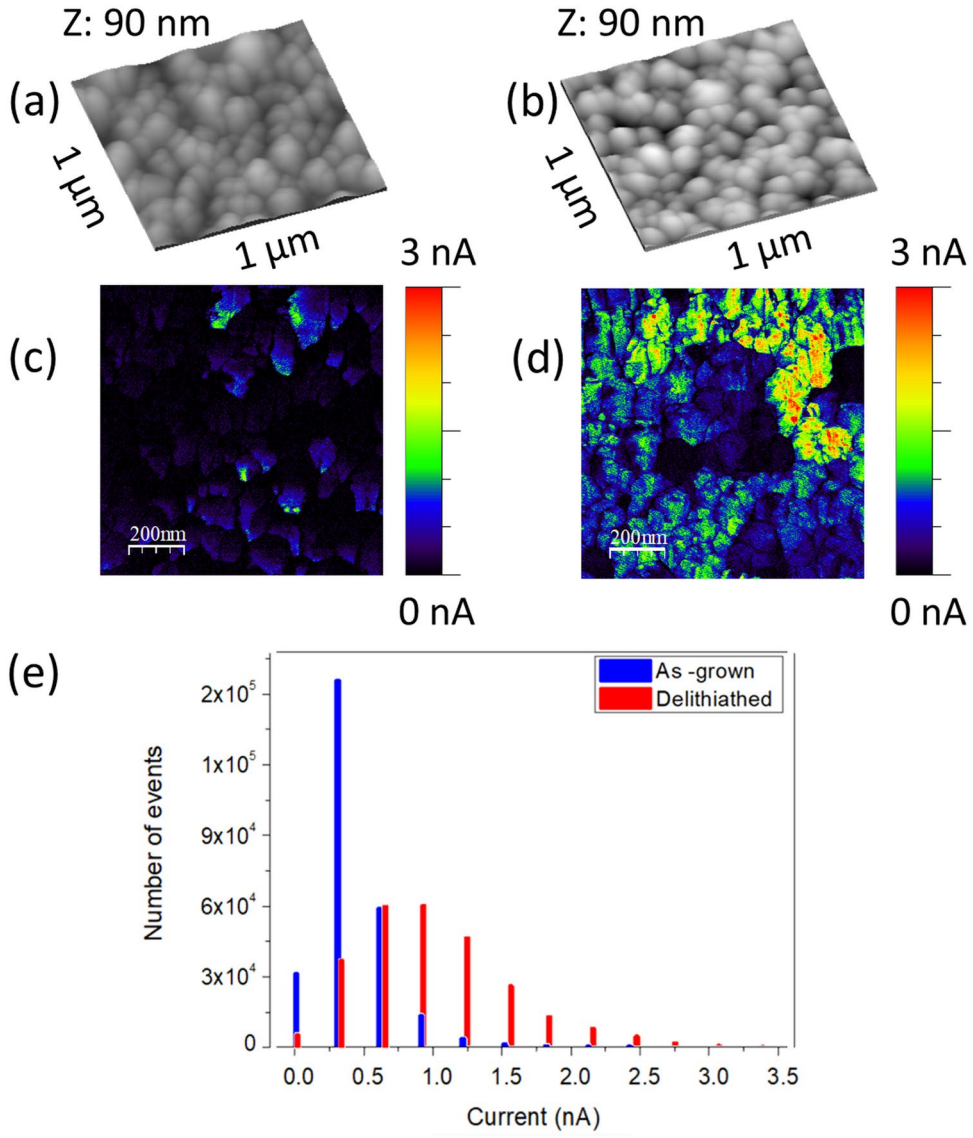

Figure 10. Topography images (**a**,**b**) and current maps (**c**,**d**) of the as-grown and delithiated samples (65 min at 10^{-2} M oxalic acid), respectively. Images size 1 µm × 1 µm. (**e**) Histogram of the current maps. Both experiments are performed with the same tip and parameters: force = 150 nN and bias voltage = − 1.5 V. Figure created with WSxM 5.0 Develop (http://www.wsxm.es)[15].

coexistence are observed, illustrating the spatial heterogeneity of the reaction. These findings support that the chemical delithiation reaction takes place predominantly at the surface of the LCO grains and is limited by the reduced mobility of Li in the granular volume of the film. As a result, regions with different Li stoichiometries can coexist. Probably, Co_3O_4 segregated to the inter-grain regions acts as a barrier to the diffusion of Li.

The suspicion that precipitated Co oxalate could contribute to this barrier is ruled out, since no distinctive signs of this compound were observed by XRD and Raman. Thus, our results do not support that the reaction of Eq. (1) describes the process. Instead, our results demonstrate that oxalic acid used in low molar concentrations (10^{-4} … 10^{-2} M) is a highly selective leaching agent for delithiation preserving the LCO structure.

Conclusions

Mild chemical delithiation of LCO thin films with oxalic acid is observed for a range of moderate acid concentrations and exposure times (Regimens I and II). Under these conditions, Li is selectively extracted after exposing LCO films to oxalic acid and the resulting Li_xCoO_2 has structural lattice constants and electrical properties similar to electrochemically delithiated LCO, albeit in a more heterogeneous manner. Deeper delithiation corresponding to increased acid concentrations and longer exposure times (Regimen III), results in a less selective Li extraction and irreversible structural damage of the LCO films. The chemical route to Li extraction provides additional opportunities to investigate delithiation while avoiding the complications associated with electrolyte breakdown and simplifying in situ measurements.

Experimental methods

LCO film growth. The samples are prepared as follows. A 10 nm Pt/Ti buffer layer is first deposited onto a Si(001) substrate capped with a 100 nm thick thermal SiO_2, using electron beam evaporation. LCO (nominal thickness ≈ 500 nm) is then deposited by magnetron sputtering in the same system, keeping the substrate at room temperature. The LCO target (Kurt J. Lesker) is sputtered with a 230 W plasma from a gas mixture of 3:1 Ar:O_2 at a static pressure of 16 mTorr. Following deposition, the LCO film is annealed in oxygen at 600 °C for 2 h in order to form the high-temperature (HT) LCO phase[13].

Chemical delithiation. Chemical extraction of Li from the polycrystalline LCO thin film is performed using a solution of oxalic acid ($C_2H_2O_4$) in distilled water and variable exposure times. Nominally, a 10^{-2} M concentration is used, but lower concentrations are also employed. As the samples are compact polycrystalline thin films of LCO, we used the drop method for the delithiation process. A drop of the solution is deposited at room conditions on top of the sample, which is maintained by surface tension of the liquid covering the entire sample surface. After exposure, the sample surface is rinsed with distilled water and analyzed immediately after.

Characterization. SEM is performed using a field-emission Philips XL-30 microscope equipped with a through lens detector (TLD). The measurements are carried out in a vacuum of 10^{-6} mbar, at an acceleration voltage of 5 kV, with magnifications ranged between 25 and 200 k.

XRD measurements are done in BM25 beamline of the ESRF using a six-circle diffractometer in vertical geometry[14] equipped with a 2 × 2 Maxipix detector on the diffractometer arm (Fig. S1 in Supplementary Information). Three circles are dedicated to the sample motion (χ, φ and θ), two circles are dedicated to the detector motion (Γ, δ), and a rotation (μ) coupled to the sample and detector motion is present. The θ-circle rotates the sample around the direction normal to the sample surface and the (χ, φ)-circles are used only for the sample alignment. The μ-circle sets the beam incidence angle, which can be varied between 0.0° and 5.0°. The Γ-detector circle performs out-of-plane measurements while the δ-circle, when $\Gamma = 0$, performs in-plane measurements. The diffractometer sphere of confusion for all axis circles is 50 μm. A photon energy of 20 keV is used for all measurements.

Micro Raman spectra are recorded in a backscattering geometry. A 532 nm excitation laser beam with power of 2 mW is focused to a 1.5 μm-diameter spot by a 50× objective lens (NA = 0.73). The scattered light is collected by the same objective lens, passes through a 532-nm long-pass edge filter, is dispersed by a single-grating monochromator and is detected with a liquid nitrogen-cooled CCD camera.

XPS experiments are performed in an ultrahigh vacuum (UHV) chamber. Mg K_α radiation (non-monochromatic) is used to excite core level photoelectrons, which are detected with a Phoibos 150 hemispherical analyzer. Before performing the XPS experiments, the LCO sample is cleaned by annealing at 500 °C in oxygen atmosphere (10^{-6} mbar). This procedure is required to remove a thin layer of surface contamination containing adventitious carbon and due to exposure to the atmosphere. The cleaning procedure is found to maintain the overall stoichiometry of the LCO sample. The Li content is measured by comparing the intensities of Li 1s and Co 3p core level peaks, which are very close to each other.

C-AFM is carried out using a Nanotec Electronica S.L. AFM tool and WSxM software[15]. We use cantilevers from Nanosensors (PtSi-NCH, PtSi coating, nominal resonance frequency of 330 kHz and spring constant of 42 Nm^{-1}) and from Budget Sensors (ElectriMulti75-G, CrPt coating, nominal resonance frequency of 75 kHz and spring constant of 2.8 Nm^{-1}). Topography and current images are taken simultaneously in contact mode at room conditions. The tip is used as a moving electrode with constant voltage applied to it while the specimen contacted by the bottom Pt/Ti electrode is grounded.

Received: 23 February 2021; Accepted: 17 May 2021
Published online: 08 June 2021

References

1. Nitta, N., Wu, F., Lee, J. T. & Yushin, G. Li-ion battery materials: Present and future. *Mater. Today* **18**, 252 (2015).
2. Goodenough, J. B. & Kim, Y. Challenges for rechargeable Li batteries. *Chem. Mater.* **22**, 587 (2010).
3. Mizushima, K., Jones, P. C., Wiseman, P. J. & Goodenough, J. B. LixCoO2 (0<x<-1): A new cathode material for batteries of high energy density. *Mater. Res. Bull.* **15**, 783 (1980).
4. Reimers, J. N. & Dahn, J. R. Electrochemical and in situ X-ray diffraction studies of lithium intercalation in LixCoO2. *J. Electrochem. Soc.* **139**, 2091 (1992).
5. Takahashi, Y. *et al.* Structure and electron density analysis of electrochemically and chemically delithiated LiCoO2 single crystals. *J. Solid State Chem.* **180**, 313 (2007).
6. Pender, J. P. *et al.* Electrode degradation in lithium-ion batteries. *ACS Nano* **14**, 1243–1295 (2020).
7. Graetz, J. *et al.* Electronic structure of chemically-delithiated LiCoO2 studied by electron energy-loss spectrometry. *J. Phys. Chem. B* **106**, 1286 (2002).
8. Gupta, R. & Manthiram, A. Chemical extraction of lithium from layered LiCoO2. *J. Solid State Chem.* **121**, 483 (1996).
9. Aaltonen, M., Peng, C., Wilson, B. P. & Lundström, M. Leaching of metals from spent lithium-ion batteries. *Recycling* **2**, 20 (2017).
10. Augustyn, V. & Manthiram, A. Effects of chemical versus electrochemical delithiation on the oxygen evolution reaction activity of nickel-rich layered LiMO2. *J. Phys. Chem. Lett.* **6**(19), 3787–3791 (2015).
11. Zeng, X., Li, J. & Shen, B. Novel approach to recover cobalt and lithium from spent lithium-ion battery using oxalic acid. *J. Hazard. Mater.* **295**, 112 (2015).
12. Rodriguez, M. H.,Suarez, D. S., Pinna, E. G., & Zeballos, C. Patent, International Application No. PCT/IB2016/056189, Publication number WO/2017/064677, Method for the acid dissolution of $LiCoO_2$ contained in spent lithium-ion batteries (2017).
13. Tintignac, S., Baddour-Hadjeana, R., Pereira-Ramosa, J. P. & Salotb, R. High performance sputtered LiCoO2 thin films obtained at a moderate annealing treatment combined to a bias effect. *Electrochim. Acta* **60**, 121–129 (2012).

14. Rubio-Zuazo, J. *et al.* The multipurpose X-ray diffraction end-station of the BM25B-SpLine synchrotron beamline at the ESRF. *Nucl. Instrum. Methods Phys.* **A716**, 23 (2013).
15. Horcas, I. *et al.* WSXM: A software for scanning probe microscopy and a tool for nanotechnology. *Rev. Sci. Instrum.* **78**, 013705 (2007).
16. Menetrier, M., Saadoune, I., Levasseur, S. & Delmas, C. The insulator-metal transition upon lithium deintercalation from LiCoO2: Electronic properties and 7Li NMR study. *J. Mater. Chem.* **9**, 1135–1140 (1999).
17. Amatucci, G. G., Tarascon, J. M. & Klein, L. CoO2, the end member of the LixCoO2 solid solution. *J. Electrochem. Soc.* **143**, 1114 (1996).
18. Milewska, A. *et al.* The nature of the nonmetal–metal transition in LixCoO2 oxide. *Solid State Ionics* **263**, 110–118 (2014).
19. Marianetti, C. A., Kotliar, G. & Ceder, G. A first-order Mott transition in LixCoO2. *Nat. Mater.* **3**, 627 (2004).
20. Deyrieux, R., Berro, C. & Peneloux, A. Contribution a l'etude des oxalates de certains metaux bivalents. *Bull. Soc. Chim. Fr.* **1**, p25-34 (1973).
21. Ren, L., Wang, P., Han, Y., Hu, C. & Wei, B. Synthesis of CoC2O4·2H2O nanorods and their thermal decomposition to Co3O4 nanoparticles. *Chem. Phys. Lett.* **476**, 78–83 (2009).
22. Dahéron, L. *et al.* Electron transfer mechanisms upon lithium deintercalation from LiCoO2 to CoO2 investigated by XPS. *Chem. Mater.* **20**, 583 (2008).
23. Lin, F. *et al.* Surface reconstruction and chemical evolution of stoichiometric layered cathode materials for lithium-ion batteries. *Nat. Comm.* **5**, 3529 (2014).
24. Miyoshi, K., Manami, K., Sasai, R., Nishigori, S. & Takeuchi, J. Electronic states realized by the interplay between Li diffusion and Co3+/Co4+ charge ordering in LixCoO2. *Phys. Rev. B* **98**, 195106 (2018).
25. Inaba, M., Iriyama, Y., Ogumi, Z., Todzuka, Y. & Tasaka, A. Raman study of layered rock-salt LiCoO2 and its electrochemical lithium deintercalation. *J. Raman Spectrosc.* **28**, 613–617 (1997).
26. Julien, C. M. & Mauger, A. In situ Raman analyses of electrode materials for Li-ion batteries. *AIMS Mater. Sci.* **5**, 650 (2018).
27. Pandey, B. K., Sukla, A., Sinha, A. K. & Gopal, R. Synthesis and characterization of cobalt oxalate nanomaterial for Li-ion battery. *Mater. Focus* **4**, 333 (2015).
28. Liu, H. L. *et al.* Electronic structure and lattice dynamics of LixCoO2 single crystals. *New J. Phys.* **17**, 103004 (2015).
29. Lebugle, A., Axelsson, U., Nyholm, R. & Mårtensson, N. Experimental L and M core level binding energies for the metals ^{22}Ti to ^{30}Zn. *Phys. Scr.* **23**, 825 (1981).
30. Motohashi, T. *et al.* Impact of lithium composition on the thermoelectric properties of the layered cobalt oxide system LixCoO2. *Phys. Rev. B* **83**, 195128 (2011).

Acknowledgements

This work has been supported by the Spanish MICINN (grant nr. FIS2017-82415-R, grant nr. MAT2017-83722-R, "María de Maeztu" Programme for Units of Excellence in R&D (CEX2018-000805-M)), within the framework of UE M-ERA.NET 2018 program under StressLIC Project (grant nr. PCI2019-103604 and PCI2019-103594) and by the Comunidad Autónoma de Madrid (grant nr. SI1/PJI/2019-00055, contract nr. PEJD-2019-PRE/IND-15769 and contract nr. PEJ-2018-AI/IND-10072). The work at Sandia National Laboratories was supported by the Laboratory-Directed Research and Development (LDRD) Program and the DOE Basic Energy Sciences Award number DE-SC0021070. Sandia National Laboratories is a multimission laboratory managed and operated by National Technology and Engineering Solutions of Sandia, LLC, a wholly owned subsidiary of Honeywell International Inc., for the U.S. Department of Energy's National Nuclear Security Administration under contract DE-NA-0003525. This paper describes objective technical results and analysis. Any subjective views or opinions that might be expressed in the paper do not necessarily represent the views of the U.S. Department of Energy or the United States Government.

Author contributions

E.S., R.B., R.C., P.S. and E.G.M. carried out and analyzed the XRD and XPS experiments. S. Q., M.J. and C.P. carried out and analyzed the C-AFM experiments. S.Q., R.B., H.P.M. and C.P. carried out and analyzed the Raman experiments. E. V. analyzed the SEM experiments. E.J.F. and A.A.T. prepared the samples. E.G.M. and C.P. devised and supervised the project. All authors discussed the results and contributed to the final manuscript.

Competing interests

The authors declare no competing interests.

Additional information

Supplementary Information The online version contains supplementary material available at https://doi.org/10.1038/s41598-021-91051-3.

Correspondence and requests for materials should be addressed to C.P.

Reprints and permissions information is available at www.nature.com/reprints.

Publisher's note Springer Nature remains neutral with regard to jurisdictional claims in published maps and institutional affiliations.